Characterisation of Deformation Process and Fracture Mechanisms of P91 Steel at 600 °C in Small Punch Tensile Testing

H. Chen[1,*], R. Yang[1], H. K. Al-Abedy[2,3], H. Li[2,4,*], W. Sun[2], and I. A. Jones[2]

[1]Department of Mechanical, Materials and Manufacturing Engineering, University of Nottingham Ningbo China, Ningbo 315100, China
[2]Faculty of Engineering, University of Nottingham, Nottingham NG7 2RD, UK
[3]College of Engineering, Wasit University, Wasit, Iraq
[4]School of Mechanical and Equipment Engineering, Hebei University of Engineering, Handan 056038, China

*Corresponding Authors.

E-mails: Hao.Chen@nottingham.edu.cn, lhzong@hebeu.edu.cn

Abstract

This paper investigates the microstructural evolution and fracture mechanism of the P91 steel during small punch tensile tests. Disc specimens, 8 mm in diameter and 0.5 mm in thickness, were tested in a small punch test rig at 600 °C using a constant displacement rate of 2 µm/s. Interrupted small punch tensile tests were performed to investigate the microstructural evolution in different deformation regimes. Deformed specimens were characterised by scanning electron microscopy and electron backscatter diffraction. Microstructure characterisation showed that block boundary alignment occurred in the plastic deformation direction, before achieving the maximum punch load. It was revealed that the martensitic structure was recovered when the tests progressed. The elongation of recovered grains occurred after achieving the maximum punch load. In addition, it was shown that the voids tended to nucleate along the recovered grain boundaries and became elongated to align with the plastic flow within the specimen.

Keywords: Small Punch Tensile Test; P91 Steel; Deformation Regimes; Void Evolution; Boundary Alignment; Fracture Mechanism

1. Introduction

In the last decade, testing techniques using miniature samples have received an ever-increasing attention in the electricity generation industry for situations where the amount of material used in the test is limited [1, 2]. Structural components in thermal power plants usually undergo creep and plasticity damage induced by volumetric inclusions such as voids and cracks. The Small Punch Tensile Test (SPTT) has been widely used as a miniature specimen test method to characterise the elastic and plastic behaviour of ductile metallic materials, with the specimen being a disc of ~8 mm diameter and ~0.5 mm thickness [3, 4]. The punch load was applied to the disc at a given constant displacement rate. The very small specimen size denotes that the SPTT can be considered as a limited-volume testing method to provide a real life evaluation of mechanical behaviours when compared with the conventional tensile test [5-8]. Moreover, the SPTT specimen can be taken directly from in-service components without significantly affecting their structural integrity [9], allowing the mechanical behaviour to be examined [10-12]. A wide range of small punch creep tests have been conducted to evaluate fracture and creep properties [13-21], in which the creep strength and minimum strain rate estimation from small punch creep tests can be correlated to the uniaxial data through finite element analysis or analytical approaches [21, 22]. In recent years even pre-cracked [23] or pre-notched specimens have been tested [24, 25]. In particular, the SPTT exhibits unique advantages in characterising power plant steels, of which the high temperature mechanical behaviour is crucial to the durability of pressure vessels.

One of the power plant steels which is of great interest is the 9Cr-1Mo steel (commercially known as P91). The microstructure of the P91 steel typically consists of prior austenite grains, martensitic packets, blocks and laths, as well as the $M_{23}C_6$ and MX precipitates [26-32], which is illustrated schematically in Figure 1. The average grain size of the austenite structure varies between 10 and 60 μm, depending on the heat treatment history [33, 34].

Each prior austenitic grain consists of a few packets which result from the martensitic transformation [35]. These packets include several blocks of martensitic laths with a typical dimension of about 4 µm [36], and the average width of martensitic laths is ~0.5 µm [37]. The micron-sized $M_{23}C_6$ carbides are mainly distributed at the prior austenite grains, block and lath boundaries, whilst the MX nano-precipitates are predominantly located within laths [31, 32]. The martensitic structure with high dislocation density provides the strengthening effects on the mechanical and creep properties. In addition, the secondary precipitates allow further precipitate strengthening by stabilising the grain boundaries and hindering dislocation movement. The distribution, volume fraction and size of the nano-precipitates in the P91 steel play a dominant role in enhancing the creep strength of this material [38, 39]. The complex structure, as described above, results in the high creep performance of the P91 material [40, 41].

However, degradation of strength may occur due to the evolution of the microstructure at elevated temperatures and over-heating over a long service exposure time [42-46]. It is widely recognised that fracture in P91 steels occurs through progressive nucleation, growth and eventual coalescence of voids. The void nucleation and coalescence events are both highly stochastic, resulting in a lack of quantitative experimental data [47, 48]. Meanwhile, most studies are based on uniaxial tests, using standard specimens where necking appears in a location that cannot be controlled. The understanding and prediction of strain and damage interactions in P91 steels remain a challenging topic. At present, the effect of multiaxial stress on void nucleation, growth and coalescence has not been fully understood and, due to this, physically based damage models cannot be adequately developed. The bi-axial loading state of SPTT appears to have the potential to examine the above physical phenomena to reveal the deformation and fracture mechanisms when the material undergoes multiaxial stresses. However, work concerned on this aspect, especially in addressing the microscopic evidence

with the deformation and fracture mechanisms of SPTT, does not appear to have been detailed yet.

Therefore, considering the significance of microstructure characteristics on the degradation of P91 during SPTT, the aim of this work is to investigate specifically the macro- and micro-structure evolution of P91 during the SPTT, in an attempt to reveal the deformation mechanisms in different deformation regimes. The results of characterising the high-temperature deformation and fracture process of the P91 steel via SPTT at 600 ℃ are presented and the deformation and fracture mechanisms in different SPTT regimes are discussed. 600 ℃ was selected as the lower end of the working temperature range for this material, as a reference for higher temperature investigations.

2. Material and Experimental Procedure

2.1. The P91 steel

The chemical composition of the as-received P91 steel is tabulated in Table 1. The as-received P91 steel was machined into a cylinder shape with 8 mm in diameter and 10 mm in length. The cylindrical bar was then normalised at 1040 °C for 40 min and tempered at 760 °C for 120 min. The heat treated bar was then sliced into disc SPTT specimens with a thickness slightly larger than 0.5 mm using wire electro-discharge machining. The specimens were then ground down to a final thickness of 0.500 ± 0.001 mm using 1200-grade silicon carbide papers, as measured by a digital micrometer.

Table 1. Chemical composition of the P91 steel (wt. %).

Fe	C	Cr	Mo	V	Nb	W	Si	Al	N	S	P
Bal	0.12	8.60	1.02	0.24	0.070	0.03	0.34	0.007	0.060	<0.002	0.017

2.2. The small punch tensile testing

A Tinius Olsen H5KS single column material testing machine was used to perform the SPTTs. A 1.0 kN load cell, which has a loading accuracy of ± 0.5 % of the applied load, is installed to measure the load transmitted to the specimen through a hemispherical punch head. The displacement of the punch was recorded as the average reading of two linear variable differential transformers, which have an accuracy of ± 0.01 mm, a resolution of 1 µm and a speed resolution of 1 µm/min. A constant displacement rate of 2 µm/s was applied to the punch and a backoff speed of 4 mm/s was applied when the specimen has failed or when the displacement of the punch has reached the setting values (for interrupted tests). The loading assembly of the small punch test rig is shown schematically in Figure 2. The radius of the punch (2) is 1.04 mm, the receiving hole diameter of the die (7) and the holder (3) is 4 mm. Nimonic 115 (from Special Metals) was used to manufacture the punch and the die set, due to its high temperature strength and low thermal expansion. The specimen (1) is clamped tightly by the screw nut (4) and the holder (3) onto the die, with a clamping stress of approximately ~300 MPa. The holder, which cannot rotate due to the locating pins (5), rests on top of the specimen and prevents the specimen from sliding. The rig, together with the specimen, is held at a constant temperature of 600 ± 1 °C in air by a furnace. Since the punch, die set and the test material exhibit low thermal expansion at this temperature, the thermal expansion of these components is neglected during the SPTT. A Type K thermocouple (6) with a working temperature range of 200 – 1250 °C is positioned close to the top surface of the specimen to control and monitor the testing temperature.

2.3. Microstructural characterisation

The microstructures of the tested specimens were examined in a Zeiss field emission gun scanning electron microscope (FEG-SEM) operated at 20 kV. The morphology of the

deformed P91 specimens was characterised using secondary electron (SE) imaging. Cross-sections of the specimens were mounted in a conductive resin, successively ground and polished to 1 µm surface finish. The polished cross-sections were chemically etched using the Vilella's reagent (5 ml hydrochloric acid, 1 g picric acid and 100 ml ethyl alcohol) and were investigated using secondary electron (SE) and backscattered electron (BSE) imaging. The semi-quantitative energy dispersive X-ray spectroscopy (EDS) was utilised for phase identification. To elucidate the evolution of grain morphology during the SPTTs, SEM-based electron backscattered diffraction (EBSD) was employed in a FEI Quanta 250 SEM equipped with an EBSD detector (Oxford Nordlys Max2). Samples for EBSD underwent a further polishing stage using colloidal silica suspension to achieve the minimum surface deformation. The EBSD system was operated at an accelerating voltage of 20 kV with a specimen tilt angle of 70 °. EBSD mappings were conducted in areas of 50 µm × 50 µm at a step size of 0.1 µm. Figure 3 depicts the initial martensitic microstructure and the EBSD Inverse Pole Figure (IPF) and grain boundary maps of the P91 steel. The boundary precipitates are visible in Figure 3a. Generally, these boundary precipitates are believed to be the $M_{23}C_6$ with M = Cr, Fe and some minor Mn. But since the steel underwent a normalisation heat treatment at 1040 °C and a tempering at 760 °C, it is possible that the MX-type (M = Nb, V and X = C, N) precipitates can also form at the boundaries. The martensitic blocks, of approximately 1.5 µm in width, can be seen in Figures 3b and 3c, where the misorientation of boundaries is above 49 °. A very limited number of high angle boundaries between 15-49 ° are noticed in Figure 3d.

3. Mechanical Behaviour

3.1. Load-displacement curves

A schematic diagram of the applied force, F, and displacement, u, of SPTT for a ductile material is shown in Figure 4a. According to Abendroth and Dymacek [49, 50], the F-u curve

can be divided into six stages, representing different deformation regimes during SPTT. Thus, to investigate the physical nature of the deformation process and the fracture behaviour of the P91 steel at 600 °C, a series of interrupted SPTTs have been carried out at a constant displacement rate of 2 µm/s. The specimens were heated up to 600 °C in approximately 60 min and stabilised for another 60 min prior to testing. Firstly, two specimens are used to perform the repeated SPTTs for the whole stroke until fracture. The load-displacement curves obtained are shown in both Figures 4b and 4c. The maximum force, F_{max}, achieved is 634 N. It is seen that the experimentally obtained load-displacement curves in Figures 4b and 4c are similar to Figure 4a. To investigate the deformation mechanisms of P91 in SPTT, the key interrupted displacements were determined based on Figure 4a. The main objective of interrupted SPTTs is to provide "In Situ" investigations into the evolution of microstructures and deformation mechanisms at each stage of the SPTT until fracture. Seven interrupted SPTTs were conducted on the P91 steel at 600 °C in Figures 4b and 4c. The interrupted displacements are set as 0.26, 0.60, 1.00, 1.25, 1.50, 1.65 and 1.74 mm respectively to represent the six deformation regimes in Figure 4a. 0.26 mm indicates the transition region from elastic deformation to plastic deformation. 0.6 mm was taken to represent plastic deformation region. 1 mm shows the deformation region where the microstructural variations start to occur. 1.25 mm was selected to approximate the displacement at maximum load. 1.5 mm was chosen as a displacement just after the maximum load to see what damage has been developed. 1.65 mm which correlates with stage V in Figure 4a is used to study the mechanisms of void nucleation and crack initiation. Finally, 1.74 mm is assumed to be the displacement very close to fracture to investigate the fracture mechanism of P91 during SPTT.

3.2. Bulk deformation behaviour

7

Figure 5 shows the SEM-SE images on the morphology of the dome-shaped P91 specimens for displacements at 0.26 mm, 0.6 mm, 1 mm and 1.25 mm. At small displacement, 0.26 mm, the dome shape starts to form when the specimen is plastically deformed as shown in Figure 5a. It is noted from Figure 4 that 0.26 mm is in the transition region between elastic and plastic deformation. Thus, plastic deformation of the P91 specimen may have already occurred. As shown in Figure 5b some cracks are formed at the top of the dome shape. These cracks are likely to have resulted from the cracking of the brittle oxide layer on the specimen surface at 600 °C. The shape of the dome becomes more evident when the displacement increases to 0.6 mm, as shown in Figure 5c. Similar features can be seen on the deformed surface, where the size of the dome increases and more cracks are developed due to the increased plastic deformation in Figure 5d. It is noticed that the cracks in the oxide layer have propagated radially from the centre of the specimen. This is also the case for the punch displacements at 1 mm and 1.25 mm in Figures 5e and 5g. The radiation of the cracks in the oxide layer indicates that the specimen is probably subjected to a tension force which leads to the stretching of the P91 specimen. Since it has been reported that the P91 is ductile in this temperature regime, the large dome-shaped deformation of the specimen during the test is produced due to the high ductility of the material [51]. It is found that the oxides of P91 are mainly chromium and iron oxides by EDS analysis. These oxides, of approximately 5 µm in thickness, are believed to be brittle due to their ceramic nature. Thus cracking of the oxide layer occurs due to the tension force developed during the punching process. Since the oxide layer is very thin, it is believed that the cracking of oxide layers would have very limited effects on the subsequent deformation and fracture of the P91 steel. But it is worth noting that the evidence of oxide cracking indicates the bi-axial stress state that the P91 specimen underwent during SPTT.

8

Figure 6 shows the SEM-SE images on the morphology of the P91 specimen at interrupted displacements of 1.5 mm, 1.65 mm and 1.74 mm. The dome shape of the specimen remains the key feature of the deformed specimens. It can be seen that the size of the dome has increased significantly due to the large displacements. It is further noticed that some voids have developed in the dome-shaped specimens in Figures 6c and 6f. These areas are near the edge of contact between the punch and specimen. The shearing between the bending and tensile stresses leads to localised material necking and thinning around the edge of contact, causing a significant decrease in the load-carrying capacity of the specimens. The voids are developed at the highly strained regions of the specimens, as highlighted in Figures 6a and 6d. This gives the crack initiation sites within the specimens. At further displacement, 1.74 mm, the fracture of the dome-shaped specimen has occurred. The voids that are seen in Figures 6a and 6d correlate with the fracture sites in Figure 6g, showing that the fracture of the specimen occurs near the edge of contact. It can be seen from the fracture surface in Figure 6i that tearing has occurred and ductile dimples were formed due to the tension force developed within the specimen.

4. Physical Characterisation of the Deformation Process in SPTT

4.1. Microstructural evolution

Figure 7 depicts the SEM cross-sectional microstructures of the above deformed P91 specimens prior to achieving the maximum punch load. It can be seen that the specimens exhibit the martensitic structure with the boundary precipitates. The small deformation after a displacement of 0.26 mm in Figure 7a exhibits a good correlation with Figure 5a, i.e. the dome shape is about to form due to the punch movement. It can be seen that the thickness of the specimen remains the same without obvious material thinning as shown in Figure 7a. No large voids have formed yet at the displacement of 0.26 mm. The dome shape becomes more

evident when the deformation of specimen increases. The alignment of blocks is not found in Figures 7b and 7d, but such evidence starts to become visible at large punch displacements as shown in Figures 7f and 7h. This indicates that the block alignment will tend to occur when the plastic deformation becomes dominant. The beginning of necking occurs in Figures 7e and 7g, due to the bending and stretching stress at the edge of contact between the punch and specimen.

Figure 8 shows the SEM cross-sectional microstructure of the P91 after achieving the maximum punch load. The dome shape has developed further due to the increased punch displacements in Figures 8a and 8c. It is noticed from Figure 8c that the necking and thinning at the edge of contact significantly progress in these specimens, where the thickness of the specimen has been further reduced due to the ongoing bending and streching stresses under the bi-axial stress state. Coarsening of the boundary precipitates is seen from Figure 8d and the lath-like microstructure becomes invisible. Meanwhile, void nucleation is found as can be seen in Figure 8b. These voids probably nucleated at the boundaries and were subsequently stretched when the punch displacements increased. Due to the large plastic deformation in these punch displacements, the voids have been deformed into elongated shapes of which the long axis is pointing to the direction of the plastic flow. A number of voids, approximately 3-5 µm across, are found in Figure 8d. Figures 8e and 8f depict the microstructure of the fracture point at the edge of contact. Some discrete and ellipsoidal voids are found close to the fracture site in Figure 8f. This indicates that the fracture of the P91 specimen tends to occur in areas which are occupied with more voids. Noting that significant material necking and thinning have occurred during this stage, together with the void nucleation and elongation, it is possible that the thinning of the specimen at the edge of contact allows the coalescence of voids to occur, resulting in the fracture of the specimen. Eventually, the tearing of the material occurs, producing the rough fracture surface.

4.2. Grain structure evolution

To further elucidate the deformation mechanisms of the P91 during SPTT, Figure 9 shows the EBSD Inverse Pole Figure (IPF) maps and the corresponding grain boundary maps at misorientations below 15 °, 15-49 ° and above 49 ° for regions near the edge of contact at displacements of 0.26, 0.6, 1.0 and 1.25 mm. Similar to the initial structure, the deformed P91 specimens exhibit the martensitic lath-like structure in Figures 9a and 9b. Since only a small displacement of 0.26 and 0.6 mm was imposed to the specimen in Figures 9a and 9b, the blocks largely maintain their original distribution without aligning to the plastic flow. When the displacement increases to 1 mm, as shown in Figure 9c and the corresponding grain boundary map, the block boundaries now start to align with the direction of the plastic flow. This is supported by the evidence that some boundaries exhibit an alignment as indicated by the arrow in Figure 9c. The alignment of the blocks is likely resulted from the continuous plastic deformation when the punch displacement increases to 1 mm. Although the alignment has occurred in this stage, some grain boundaries still remain randomly distributed. When the displacement increases further to 1 and 1.25 mm, evidence of boundary alignment can be seen in Figure 9d. No preferred grain orientation has been developed yet. This means that the grain structure of the P91 specimen mainly undergoes boundary alignment along the direction of plastic flow at these deformation regimes. An increased number of high angle boundaries between 15-49 ° is also noticed from the grain boundary maps in Figures 9c and 9d. Since these high angle boundaries usually indicate the recovered ferritic structure [52], it is possible that the martensitic structure has been partially recovered. Indeed, the martensitic lath-like features can be seen clearly in Figures 9a and 9b but some equiaxed grains start to become visible in Figures 9c and 9d.

Figure 10 shows the EBSD Inverse Pole Figure (IPF) maps and the corresponding grain boundary maps at misorientations below 15 °, 15-49 ° and above 49 ° at the edge of contact for SPTT displacements at 1.5, 1.65 and 1.74 mm. It is further noticed that the number of high angle grain boundaries between 15-49 ° has been increased significantly from the grain boundary maps in Figure 10. This means that the initial martensitic structure has been greatly recovered to a ferritic structure. This is supported by the evidence that more equiaxed grains are formed at this stage and the lath-like microstructure has almost diminished. Since the boundary alignment has already occurred in the previous deformation stages, the behaviour in this regime is dominated by the elongation of the recovered grains.

It can be seen from Figure 10c that the fracture site passed through the edge of contact where the structure has been recovered. To demonstrate the preference of void nucleation, Figure 11 shows the SEM-SE micrograph and the EBSD Image Quality (IQ) map, Inverse Pole Figure (IPF) map and the corresponding grain boundary map at misorientations below 15 °, 15-49 ° and above 49 ° for an area close to the fracture point. The voids that formed close to the fracture site have become aligned with the plastic flow direction, and exhibit an elongated morphology. Meanwhile, a clear recovered equiaxed structure with elongated grains is evident from the EBSD mappings in Figure 11. It is found that the voids are mainly distributed along the grain boundaries of the recovered grains, as evidenced from the grain boundary map, indicating that the voids nucleate preferentially at the recovered grain boundaries.

5. Discussion

5.1. Deformation regimes and plasticity energy

The deformation energy which is calculated by the area below the small punch test curve can be used to correlate the deformation process at different SPTT stages [50]. The percentage of

deformation energy at different stages of SPTT is summarised in Figure 12a. It can be seen that over 65 % of the energy is consumed before the maximum load is reached. Since the continuous movement of the punch results in progressive material necking and thinning at the edge of contact, Figure 12b presents the evolution of the specimen thickness at the edge of contact. The minimum thickness at the edge of contact was taken to represent how the material thinning occurs during the SPTT. It can be seen that the significant material thinning primarily occurs after the maximum load is achieved. This behaviour is similar to that observed in uniaxial tensile testing in which the necking occurs after the ultimate tensile stress. The significant thinning at the edge of contact indicates that the specimen starts to fracture, which shows good consistency with Figure 8. The evolution of the specimen thickness at the edge of contact, t in µm, is empirically derived from Figure 12b, as given below in Eq. (1) as a function of displacement (u in mm).

$$t_{(\mu m)} = -226u^2 + 147u + 469 \qquad (1)$$

To further demonstrate the specimen response during the SPTT, Figure 13 gives the schematic diagram of deformation of the specimen at different stages, from the initial plastic deformation to the necking at failure. Stage II represents the transition zone from elastic to plastic deformation, in which plastic deformation occurs in the local contact zone between the punch tip and the specimen, stretching the material into the receiving die. Stage III represents homogeneous plastic deformation and the specimen thickness reduces uniformly in the deformation zone (as shown in Figures 5a, 5c and 5e and Figures 7a, 7c and 7e for punch displacements from 0.26 mm to 1.0 mm). The energy required for the initial elastic deformation (Stage I in Figure 12a) is quite small (2.1 %) but gradually increases with displacements in the plastic deformation regimes. In Stage III, the energy consumed is more than 45 % of the total energy, indicating that the P91 exhibits a good toughness. The thickness of specimen reduces at localised circular band near the contact edge between the

punch and specimen in Stage IV (as shown in Figure 5g and Figure 7g), in which circumferential necking occurs and the energy consumed is around 20 %, where the rate of energy decreases in this stage. It is possible that material thinning and void nucleation start to occur in this stage (Figure 7g), resulting in a decrease in plasticity deformation of the P91 specimen. In Stage V, the continuous plastic deformation and the on-going material necking and thinning lead to the formation of large voids near the edge of contact, as shown in Figures 6a and 6d and Figures 8a and 8c, in which the nucleation and elongation of voids lead to the void coalescence and the point necking occur in the circumferential necking area. Since the continuous necking and thinning occurs with the punch movement, the energy consumed is about 29 % in this deformation regime. Finally, the material is torn when approaching the failure in Stage VI (as shown in Figure 6g and Figure 8e), in which the energy consumed is only 4.1 % of the total energy due to the area at the contact edge is reduced as failure is approached.

5.2. Deformation and facture mechanisms

From Figures 9 and 10, it can be seen that the grain behaviour of the P91 during the SPTT can be divided into two regimes, namely block boundary alignment before the maximum load (Stages I-IV in Figures 12 and 13) and elongation of recovered grains after the maximum load (Stages V-VI in Figures 12 and 13). This is schematically illustrated in Figure 14. Before achieving the maximum load, the P91 specimens gradually deform with the punch displacements. The "stiffening effect" of the specimen during SPTT allows the load that is required to further deform the specimen to increase (Stages II-III). During the SPTT, the regions along the edge of contact between the punch and specimen are subjected to the "stretching effect" when the punch starts to deform the specimen, leading to the circumferential necking (Stage IV). In the alignment stage, the martensitic blocks are aligned

with the plastic flow from Figures 14a to 14b. This is evidenced by the alignment of the block boundaries in Figure 9. The morphology of the grains maintains the original morphology without significant changes to the grain orientations. This behaviour of grain alignment dominates the deformation mechanism in Stages II-IV. Meanwhile, the recovery and elongation occurs after the maximum load in Stages V-VI. Since the blocks have already been aligned along the plastic flow direction, the load required to further deform the sample decreases, as indeed seen in Figures 4b and 4c. Although void nucleation is seen in Figure 8d, the number of voids is quite limited. Due to the recovery of the martensitic structure, the lath-like features have been changed to a more equiaxed ferritic structure. During this stage, the recovered grains have become elongated along the plastic flow direction, as seen in Figure 10c. Therefore, in the deformation stage after the maximum load (Stages V-VI), the deformation mechanism is realised by the elongation of the recovered grains in Figure 14c. Similar findings have also been reported by others on the alignment of grains of a MA956 ODS steel during SPTT [53] and the recovery of martensitic structure [52], which shows good consistency with this work.

Since the voids nucleation and coalescence occur during the SPTT, the size of the voids near the edge of contact is compared. The diameter is quoted for spherical or nearly spherical voids whilst the long axis is quoted for the ellipsoidal voids. It can be seen from Figure 7 that the diameter of the spherical voids is approximately 1 µm. The size of the voids does not change significantly before the maximum load. The small displacements of 0.26, 0.6 and 1 mm would not lead to the formation of the voids. When the displacements increase further, especially after the maximum load, small and discrete sub-micron voids start to become elongated. It is indicated from Figure 11 that the void nucleation occurs at boundaries of the recovered grains. Since the localised shearing and stretching are believed to be effective in facilitating the growth of the voids during the SPTT, especially at larger displacements, the

voids are subjected to the same stress state as the bulk material under the stretching effects during the SPTT. As a result, the voids are elongated to become ellipsoidal shapes, as seen in Figure 8. The size of the voids is approximately 5 µm or even larger when the deformation of specimen increases to 1.74 mm as shown in Figure 8f. Some large voids are also developed during this stage, indicating a possible coalescence of the voids during the SPTT. Since it is noticed from Figures 7 and 8 that the voids have grown significantly after the maximum load, it is thus believed that the fracture mechanism consists of the void elongation and coalescence along the recovered grain boundaries near the fracture site in Figure 14d.

6. Conclusions

The interrupted small punch tensile tests of P91 were performed at 600 °C to investigate the deformation and fracture mechanisms. The bulk deformation behaviour and the microstructure evolution during the SPTTs were characterised. The main conclusions are drawn as follows:

- The bulk deformation behaviour of the P91 during SPTT exhibits the typical six deformation regimes. It is found that over 65 % of the plasticity energy is consumed before the maximum punch load. From the microstructure evolution, it is shown that significant necking and thinning occur after the maximum punch load.

- It is shown from the microstructure evolution that the martensitic blocks maintain their original morphology prior to achieving the maximum load in SPTT, but a tendency to align themselves along the stretching direction is observed.

- Significant recovery occurs after achieving the maximum load, exhibiting a more equiaxed structure with recovered ferritic grains. The recovered grains are elongated along the plastic flow direction. It is further found that the voids nucleate preferentially along the recovered grain boundaries.

16

- A number of voids are developed close to the fracture site and the voids have been developed into nearly ellipsoidal shapes. The final fracture of the P91 specimen is believed to be a combination of void coalescence at the recovered grain boundaries and tearing at the contact edge between the punch and specimen.

Declaration of interest

None.

Data availability

The raw/processed data required to reproduce these findings cannot be shared at this time as the data also forms part of an ongoing study.

References

[1] A. Morris, B. Cacciapuoti, W. Sun, The role of small specimen creep testing within a life assessment framework for high temperature power plant, Int. Mater. Rev. 63 (2018) 102-137.

[2] T.H. Hyde, W. Sun, J.A. Williams, Requirements for and use of miniature test specimens to provide mechanical and creep properties of materials: a review, Int. Mater. Rev. 52 (2007) 213-255.

[3] D. Blagoeva, R. Hurst, Application of the CEN (European Committee for Standardization) small punch creep testing code of practice to a representative repair welded P91 pipe, Mater. Sci. Eng. : A 510 (2009) 219-223.

[4] M. Bruchhausen, T. Austin, S. Holmström, E. Altstadt, P. Dymacek, S. Jeffs, R. Lancaster, R. Lacalle, K. Matocha, J. Petzová, European Standard on Small Punch Testing of Metallic Materials, ASME 2017 Pressure Vessels and Piping Conference, (2017).

[5] N. Panayotou, R. Puigh, E. Opperman, Miniature specimen tensile data for high energy neutron source experiments, J. Nucl. Mater. 104 (1981) 1523-1526.

[6] M. Madia, S. Foletti, G. Torsello, A. Cammi, On the applicability of the small punch test to the characterization of the 1CrMoV aged steel: Mechanical testing and numerical analysis, Eng. Fail. Anal. 34 (2013) 189-203.

[7] G. Lucas, The development of small specimen mechanical test techniques, J. Nucl. Mater. 117 (1983) 327-339.

[8] J.S. Ha, E. Fleury, Small punch tests on steels for steam power plant (I), Ksme Int. J. 12 (1998) 818.

[9] C. Rodríguez, M. Fernández, J. Cabezas, T. García, F. Belzunce, The use of the small punch test to solve practical engineering problems, Theor. Appl. Fract. Mec. 86 (2016) 109-116.

[10] C. Rodríguez, J. García, E. Cárdenas, F. Belzunce, C. Betegón, Mechanical properties characterization of heat-affected zone using the small punch test, Weld. J. 88 (2009) 188-192.

[11] M. Fernández, C. Rodríguez, F. Belzunce, T. García, Use of small punch test to estimate the mechanical properties of powder metallurgy products employed in the automotive industry, Powder Metall. 58 (2015) 171-177.

[12] H. Chen, G.A. Jackson, W. Sun, An Overview of Using Small Punch Testing for Mechanical Characterization of MCrAlY Bond Coats, J. Therm. Spray Technol. 26 (2017) 1222-1238.

[13] Y. Shindo, Y. Yamaguchi, K. Horiguchi, Small punch testing for determining the cryogenic fracture properties of 304 and 316 austenitic stainless steels in a high magnetic field, Cryogenics 44 (2004) 789-792.

[14] H. Chen, T.H. Hyde, K.T. Voisey, D.G. McCartney, Application of small punch creep testing to a thermally sprayed CoNiCrAlY bond coat, Mater. Sci. Eng. A 585 (2013) 205-213.

[15] X. Mao, H. Takahashi, Development of a further-miniaturized specimen of 3 mm diameter for tem disk (ø 3 mm) small punch tests, J. Nucl. Mater. 150 (1987) 42-52.

[16] H. Chen, Microstructure characterisation of un-melted particles in a plasma sprayed CoNiCrAlY coating, Mater. Charact. 136 (2018) 444-451.

[17] X. Ling, Y. Zheng, Y. You, Y. Chen, Creep damage in small punch creep specimens of Type 304 stainless steel, Int. J. Pres. Ves. Pip. 84 (2007) 304-309.

[18] F. Dobeš, K. Milička, Comparison of conventional and small punch creep tests of mechanically alloyed Al–C–O alloys, Mater. Charact. 59 (2008) 961-964.

[19] J. Bulloch, A study concerning material fracture toughness and some small punch test data for low alloy steels, Eng. Fail. Anal. 11 (2004) 635-653.

[20] H. Chen, A. Rushworth, W. Sun, J. He, H. Guo, Some considerations in using the small punch testing for thermally sprayed CoNiCrAlY coatings, Surf. Coat. Technol. 357 (2019) 684-690.

[21] S. Holmström, Y. Li, P. Dymacek, E. Vacchieri, S.P. Jeffs, R.J. Lancaster, D. Omacht, Z. Kubon, E. Anelli, J. Rantala, A. Tonti, S. Komazaki, Naveena, M. Bruchhausen, R.C. Hurst, P. Hähner, M. Richardson, D. Andres, Creep strength and minimum strain rate estimation from Small Punch Creep tests, Mater. Sci. Eng. A 731 (2018) 161-172.

[22] T.H. Hyde, M. Stoyanov, W. Sun, C.J. Hyde, On the interpretation of results from small punch creep tests, J. Strain Anal. Eng. Des. 45 (2010) 141-164.

[23] I. Cuesta, J. Alegre, Determination of the fracture toughness by applying a structural integrity approach to pre-cracked small punch test specimens, Eng. Fract. Mech. 78 (2011) 289-300.

[24] Y. Xu, K. Guan, Evaluation of fracture toughness by notched small punch tests with Weibull stress method, Mater. Design 51 (2013) 605-611.

[25] I. Cuesta, C. Rodriquez, F. Belzunce, J. Alegre, Analysis of different techniques for obtaining pre-cracked/notched small punch test specimens, Eng. Fail. Anal. 18 (2011) 2282-2287.

[26] R. Barrett, P. O'Donoghue, S. Leen, A dislocation-based model for high temperature cyclic viscoplasticity of 9–12Cr steels, Comp. Mater. Sci. 92 (2014) 286-297.

[27] H.K. Al-Abedy, I.A. Jones, W. Sun, Small punch creep property evaluation by finite element of Kocks-Mecking-Estrin model for P91 at elevated temperature, Theor. Appl. Fract. Mech. 98 (2018) 244-254.

[28] S. Qiao, Y. Wei, H. Xu, H. Cui, F. Lu, The evolution behavior of second phases during long-term creep rupture process for modified 9Cr-1.5Mo-1Co steel welded joint, Mater. Charact. 151 (2019) 318-331.

[29] K. Guguloth, N. Roy, Study on the creep deformation behavior and characterization of 9Cr-1Mo-V-Nb steel at elevated temperatures, Mater. Charact. 146 (2018) 279-298.

[30] V. Sklenička, K. Kuchařová, M. Svoboda, L. Kloc, Burši, x, J. k, A. Kroupa, Long-term creep behavior of 9–12%Cr power plant steels, Mater. Charact. 51 (2003) 35-48.

[31] J. Vivas, C. Capdevila, E. Altstadt, M. Houska, M. Serrano, D. De-Castro, D. San-Martín, Effect of ausforming temperature on creep strength of G91 investigated by means of Small Punch Creep Tests, Mater. Sci. Eng. A 728 (2018) 259-265.

[32] J. Vivas, C. Capdevila, E. Altstadt, M. Houska, D. San-Martín, Importance of austenitization temperature and ausforming on creep strength in 9Cr ferritic/martensitic steel, Scripta Mater. 153 (2018) 14-18.

[33] B. Fournier, M. Sauzay, F. Barcelo, E. Rauch, A. Renault, T. Cozzika, L. Dupuy, A. Pineau, Creep-fatigue interactions in a 9 Pct Cr-1 Pct Mo martensitic steel: part II. Microstructural evolutions, Metall. Mater. Trans. A 40 (2009) 330-341.

[34] V. Sklenicka, K. Kucharova, M. Svobodova, P. Kral, M. Kvapilova, J. Dvorak, The effect of a prior short-term ageing on mechanical and creep properties of P92 steel, Mater. Charact. 136 (2018) 388-397.

[35] V. Shankar, M. Valsan, K.B.S. Rao, R. Kannan, S. Mannan, S. Pathak, Low cycle fatigue behavior and microstructural evolution of modified 9Cr–1Mo ferritic steel, Mater. Sci. Eng. : A 437 (2006) 413-422.

[36] M. Sauzay, B. Fournier, M. Mottot, A. Pineau, I. Monnet, Cyclic softening of martensitic steels at high temperature—Experiments and physically based modelling, Mater. Sci. Eng. : A 483 (2008) 410-414.

[37] C.G. Panait, A. Zielińska-Lipiec, T. Koziel, A. Czyrska-Filemonowicz, A.-F. Gourgues-Lorenzon, W. Bendick, Evolution of dislocation density, size of subgrains and MX-type

precipitates in a P91 steel during creep and during thermal ageing at 600 C for more than 100,000 h, Mater. Sci. Eng. : A 527 (2010) 4062-4069.

[38] A. Benaarbia, X. Xu, W. Sun, A.A. Becker, M.A.E. Jepson, Investigation of short-term creep deformation mechanisms in MarBN steel at elevated temperatures, Mater. Sci. Eng. A 734 (2018) 491-505.

[39] C.G. Panait, A. Zielińska-Lipiec, T. Koziel, A. Czyrska-Filemonowicz, A.-F. Gourgues-Lorenzon, W. Bendick, Evolution of dislocation density, size of subgrains and MX-type precipitates in a P91 steel during creep and during thermal ageing at 600°C for more than 100,000h, Mater. Sci. Eng. A 527 (2010) 4062-4069.

[40] F. Abe, Creep Behavior, Deformation Mechanisms, and Creep Life of Mod.9Cr-1Mo Steel, Metall. Mater. Trans. A 46 (2015) 5610-5625.

[41] F. Abe, Progress in Creep-Resistant Steels for High Efficiency Coal-Fired Power Plants, Journal of Pressure Vessel Technology, Transactions of the ASME 138 (2016).

[42] C. Pandey, A. Giri, M. Mahapatra, Evolution of phases in P91 steel in various heat treatment conditions and their effect on microstructure stability and mechanical properties, Mater. Sci. Eng. : A 664 (2016) 58-74.

[43] S.D. Yadav, S. Kalácska, M. Dománková, D.C. Yubero, R. Resel, I. Groma, C. Beal, B. Sonderegger, C. Sommitsch, C. Poletti, Evolution of the substructure of a novel 12% Cr steel under creep conditions, Mater. Charact. 115 (2016) 23-31.

[44] A.K. Metya, M. Ghosh, N. Parida, K. Balasubramaniam, Effect of tempering temperatures on nonlinear Lamb wave signal of modified 9Cr–1Mo steel, Mater. Charact. 107 (2015) 14-22.

[45] X. Zhang, Y. Zeng, W. Cai, Z. Wang, W. Li, Study on the softening mechanism of P91 steel, Mater. Sci. Eng. A 728 (2018) 63-71.

[46] Y. Wu, E. Bousser, T. Schmitt, N. Tarfa, F. Khelfaoui, R. René, J.-E. Klemberg-Sapieha, M. Brochu, Thermal stability of a Stellite/steel hardfacing interface during long-term aging, Mater. Charact. 154 (2019) 181-192.

[47] L. An, Q. Xu, D. Xu, Z. Lu, Review of creep deformation and rupture mechanism of P91 alloy for the development of creep damage constitutive equations under low stress level, The 10th International Conference on Science Computing, USA, (2013).

[48] V. Gaffard, J. Besson, A.-F. Gourgues-Lorenzon, Creep failure model of a tempered martensitic stainless steel integrating multiple deformation and damage mechanisms, Int. J. Fract. 133 (2005) 139-166.

[49] M. Abendroth, FEM analysis of small punch tests, Key Eng. Mat. 734 (2017) 23-36.

[50] P. Dymáček, Recent developments in small punch testing: Applications at elevated temperatures, Theor. Appl. Fract. Mech. 86A (2016) 25-33.

[51] B. Cacciapuoti, W. Sun, D.G. McCartney, A study on the evolution of the contact angle of small punch creep test of ductile materials, Int. J. Pressure Vessels Piping 145 (2016) 60-74.

[52] J. Vivas, C. Capdevila, E. Altstadt, M. Houska, I. Sabirov, D. San-Martín, Microstructural Degradation and Creep Fracture Behavior of Conventionally and Thermomechanically Treated 9% Chromium Heat Resistant Steel, Metals and Materials International 25 (2019) 343-352.

[53] K. Turba, R.C. Hurst, P. Hähner, Anisotropic mechanical properties of the MA956 ODS steel characterized by the small punch testing technique, J. Nucl. Mater. 428 (2012) 76-81.
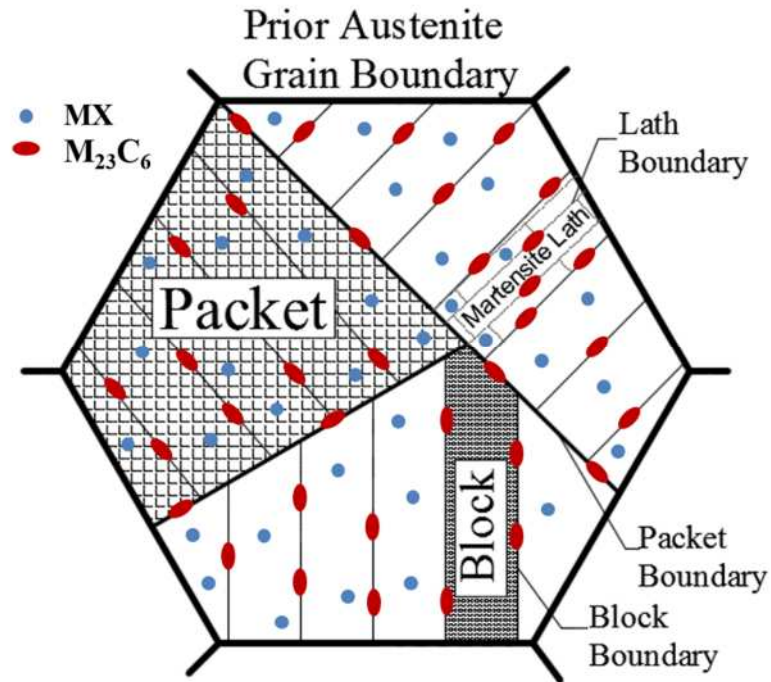
Figure 1. A schematic diagram showing the typical microstructure of the P91 steel.
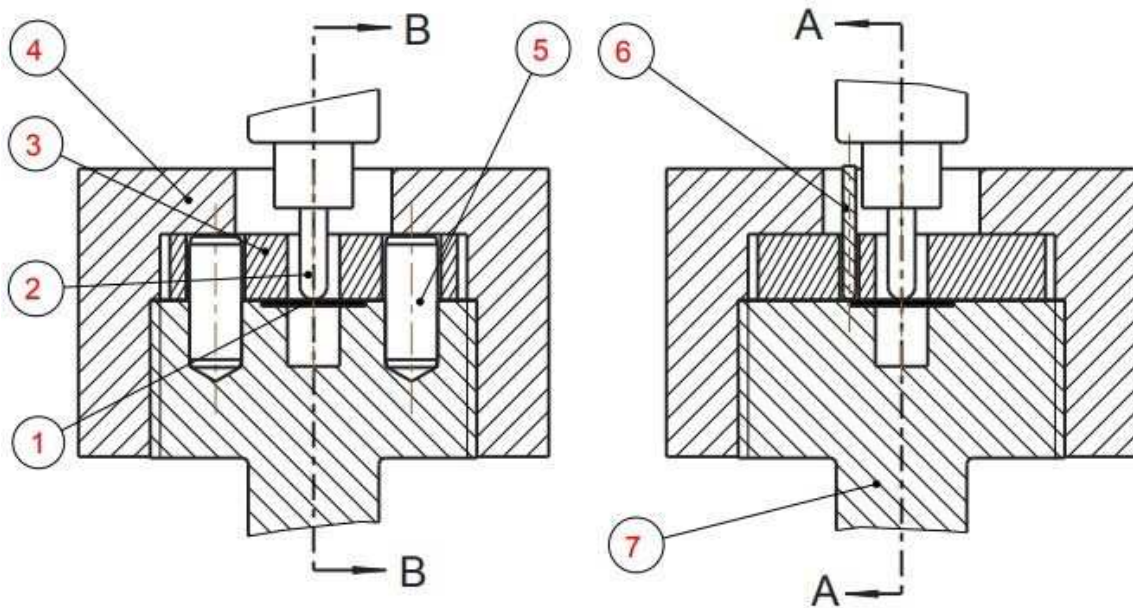
Figure 2. Detailed drawing of the loading assembly: 1. Specimen, 2. Hemispherical punch, 3. Holder, 4. Screwing nut, 5. Locating pins, 6. Thermocouple, and 7. Die.
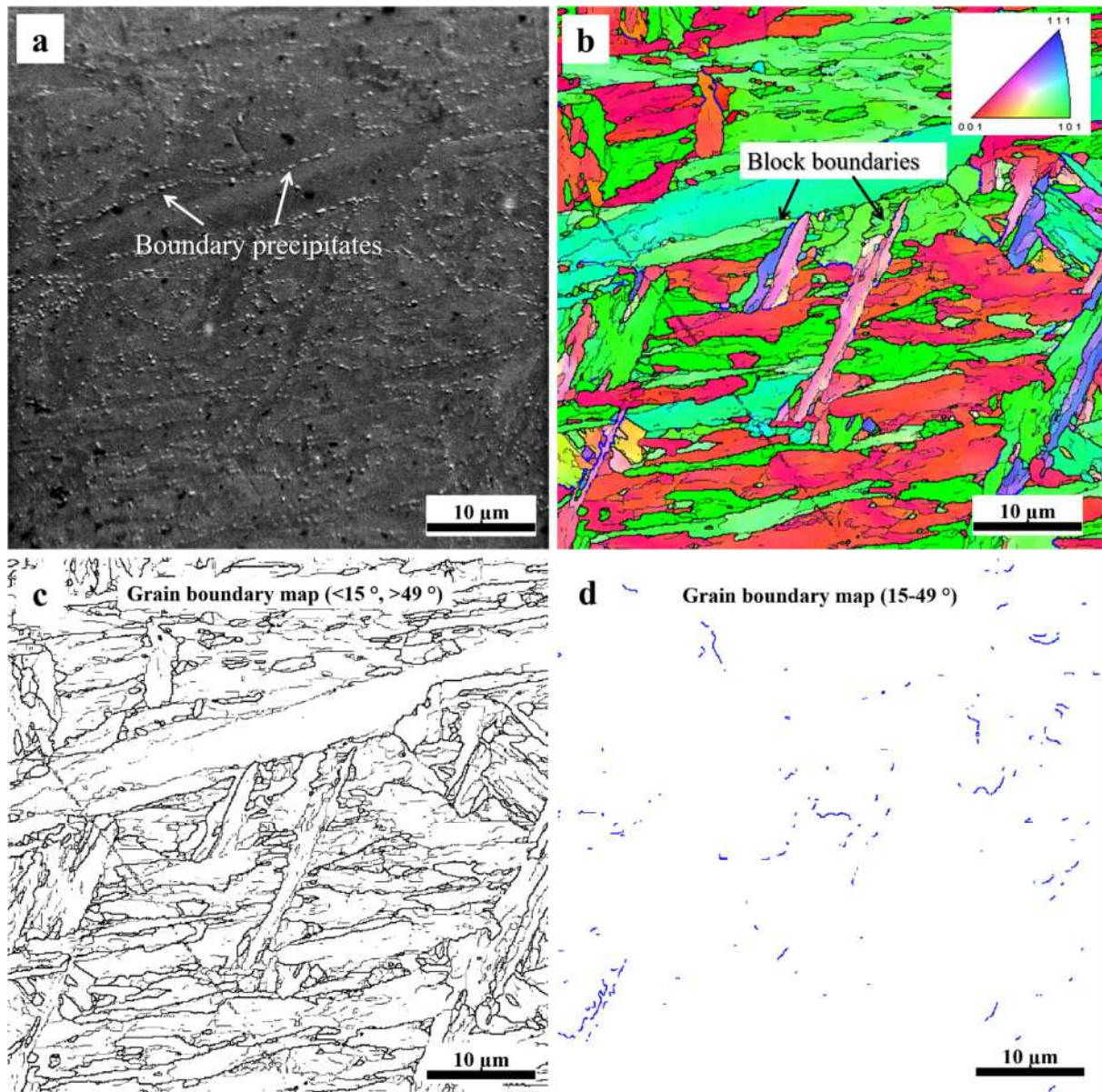
Figure 3. SEM-SE image (a) showing the initial martensitic structure with $M_{23}C_6$ or MX boundary precipitates and EBSD-IPF (b), grain boundary maps for misorientations of <15 ° and >49 ° (c) and between 15-49 ° (d) showing the grain structure. The grey lines and black lines in (c) represent the misorientations <15 ° and >49 ° respectively. The blue lines in (d) represent the misorientations between 15-49 °.
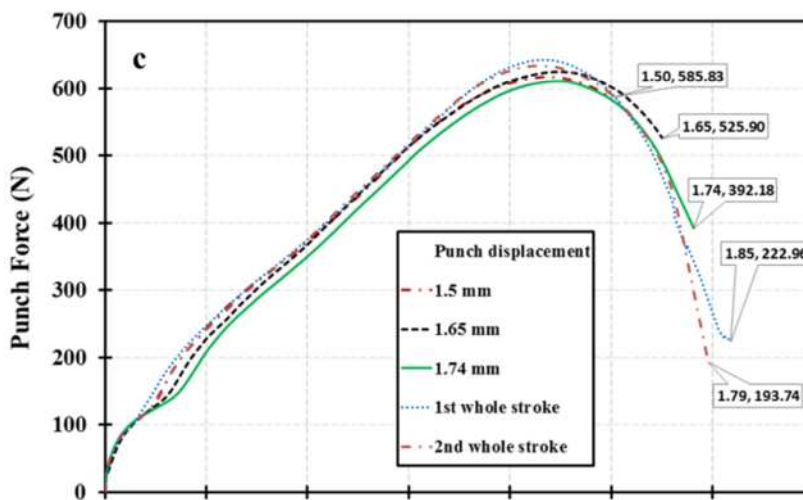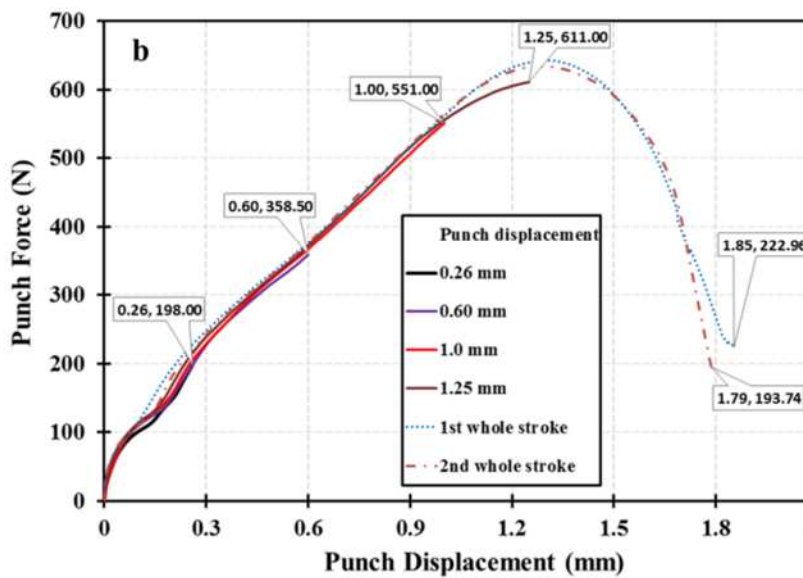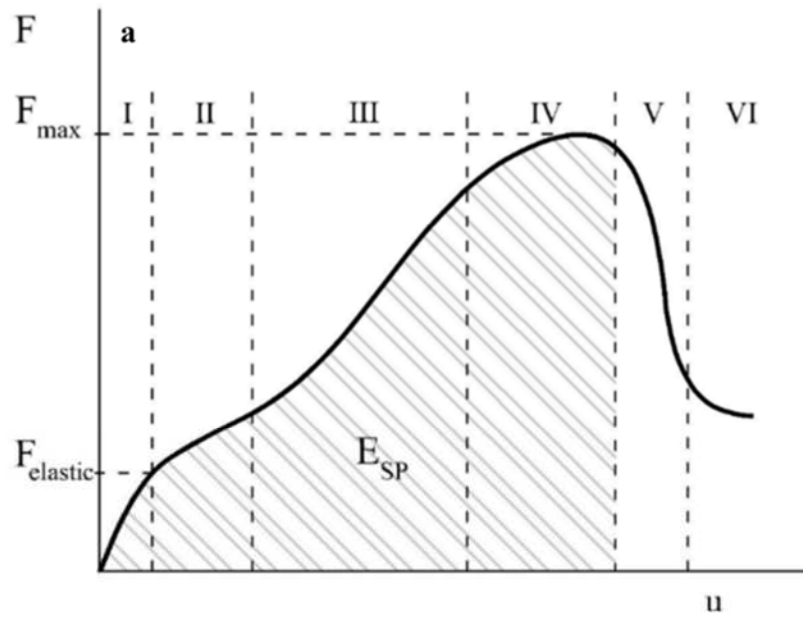
Figure 4. The schematic diagram of the SPTT load-displacement curve (a), the experimental load-displacement curves at interrupted displacements of 0.26, 0.60, 1.00 and 1.25 mm (b) and 1.50, 1.65 and 1.74 mm (c). Two whole strokes of SPTTs are included in both b and c.
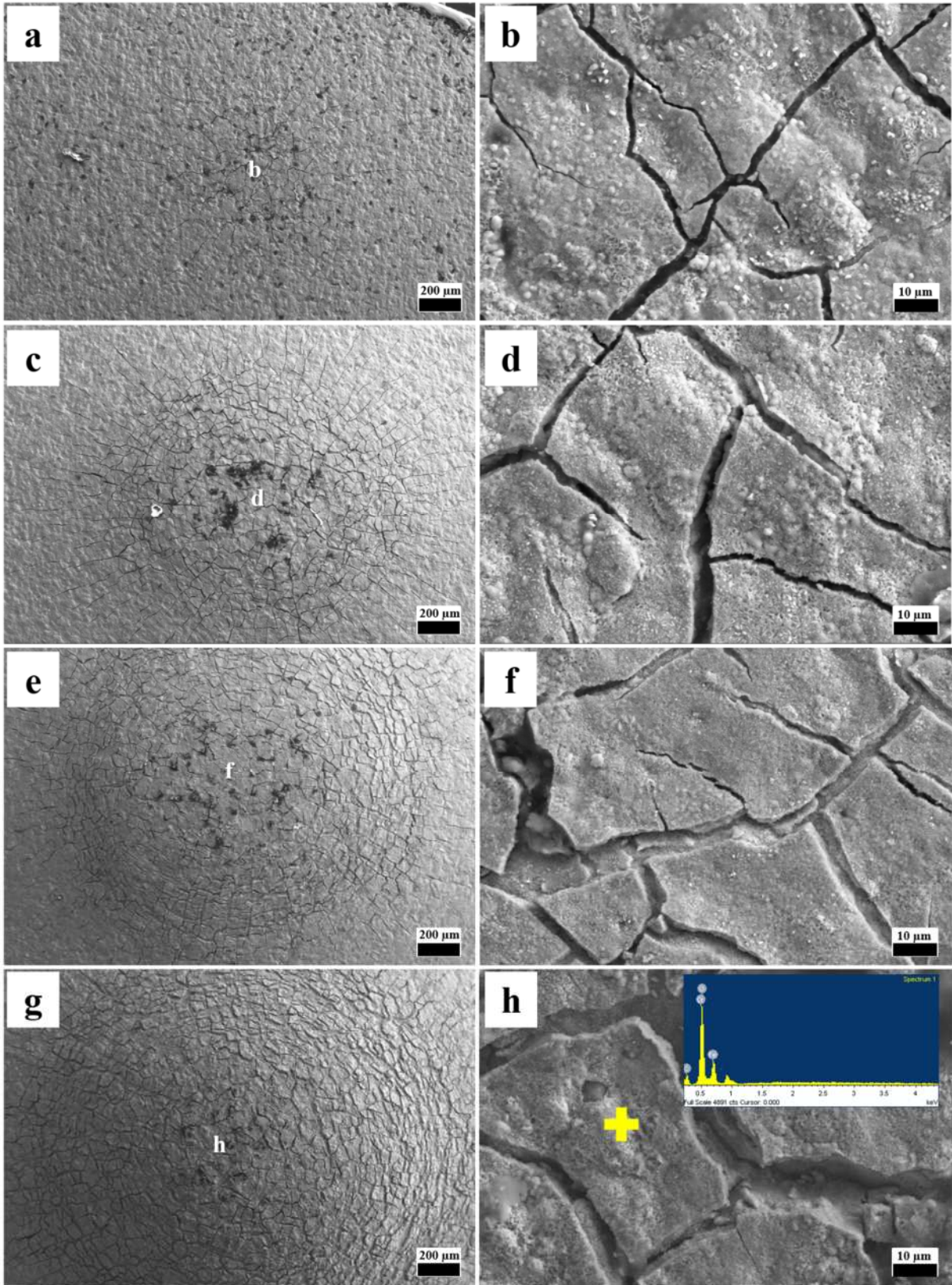
Figure 5. The SEM-SE images showing the morphology of the deformed P91 specimens at 0.26 mm (a and b), 0.6 mm (c and d), 1.0 mm (e and f) and 1.25 mm (g and h). The centre of the disc is marked as b, d, f and h.
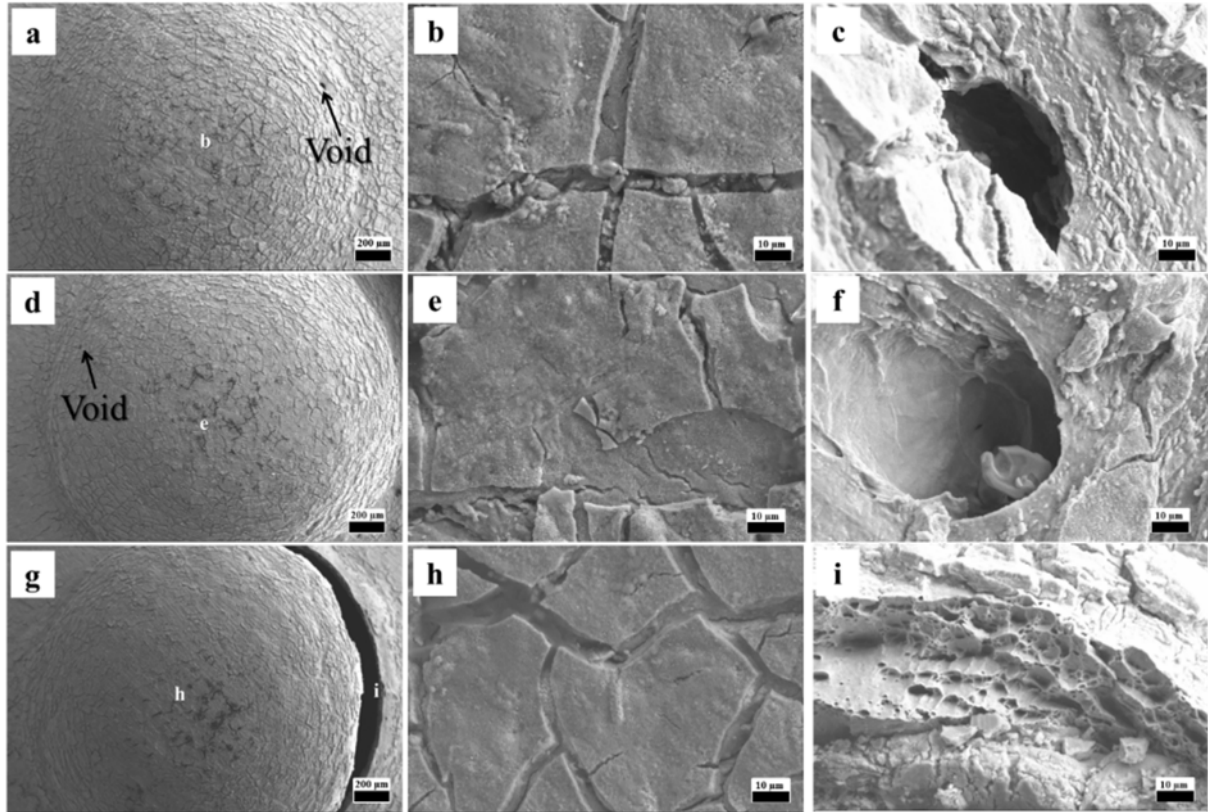
Figure 6. The SEM-SE images showing the morphology of the deformed specimens at interrupted displacements of 1.5 mm (a, b and c), 1.65 mm (d, e and f) and 1.74 mm (g, h and i). The centre of the disc is marked as b, e and h.
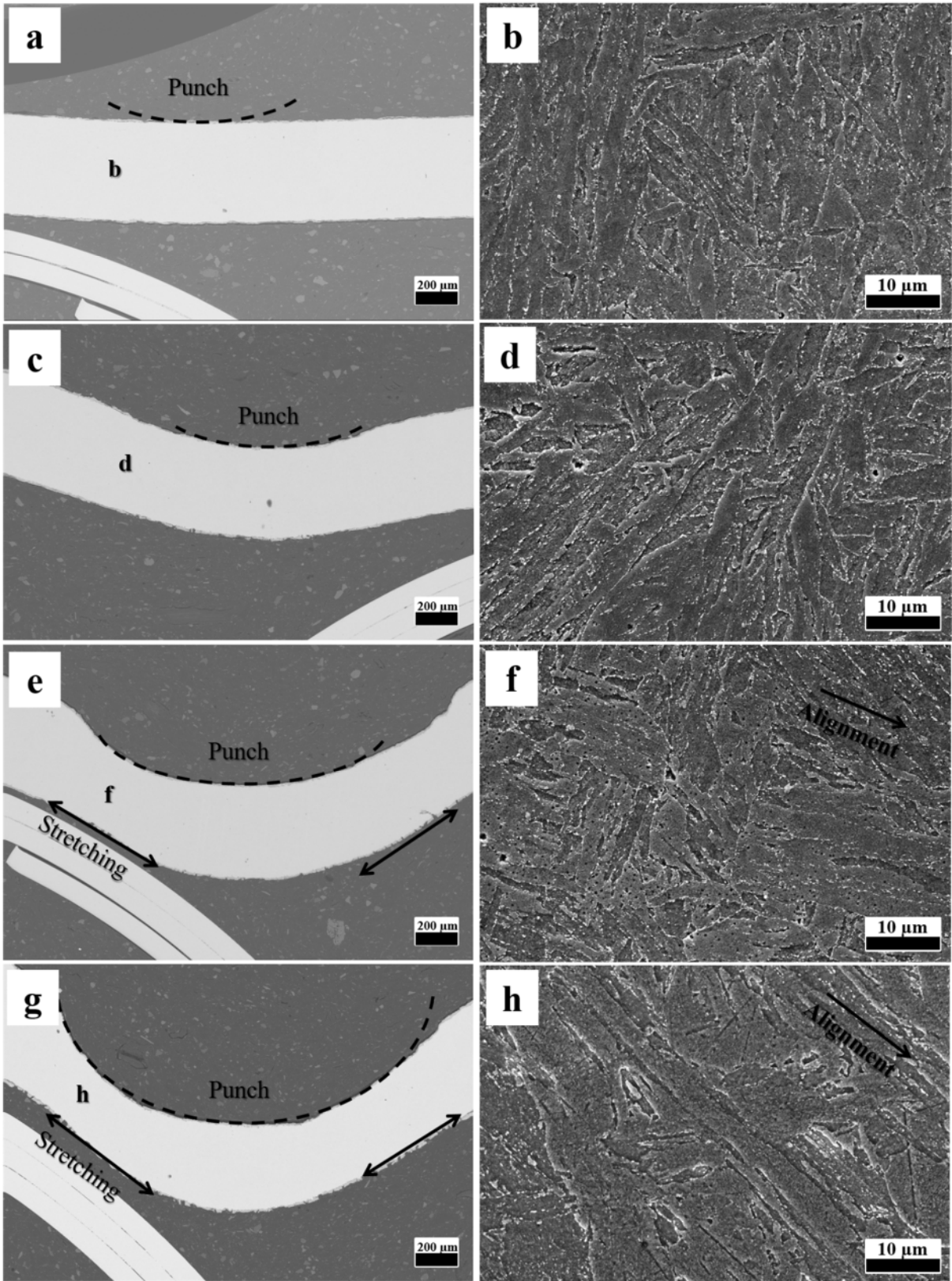
Figure 7. The SEM-SE images showing the cross-sectional microstructure of the deformed specimens at interrupted displacements of 0.26 mm (a and b), 0.6 mm (c and d), 1.0 mm (e and f) and 1.25 mm (g and h).
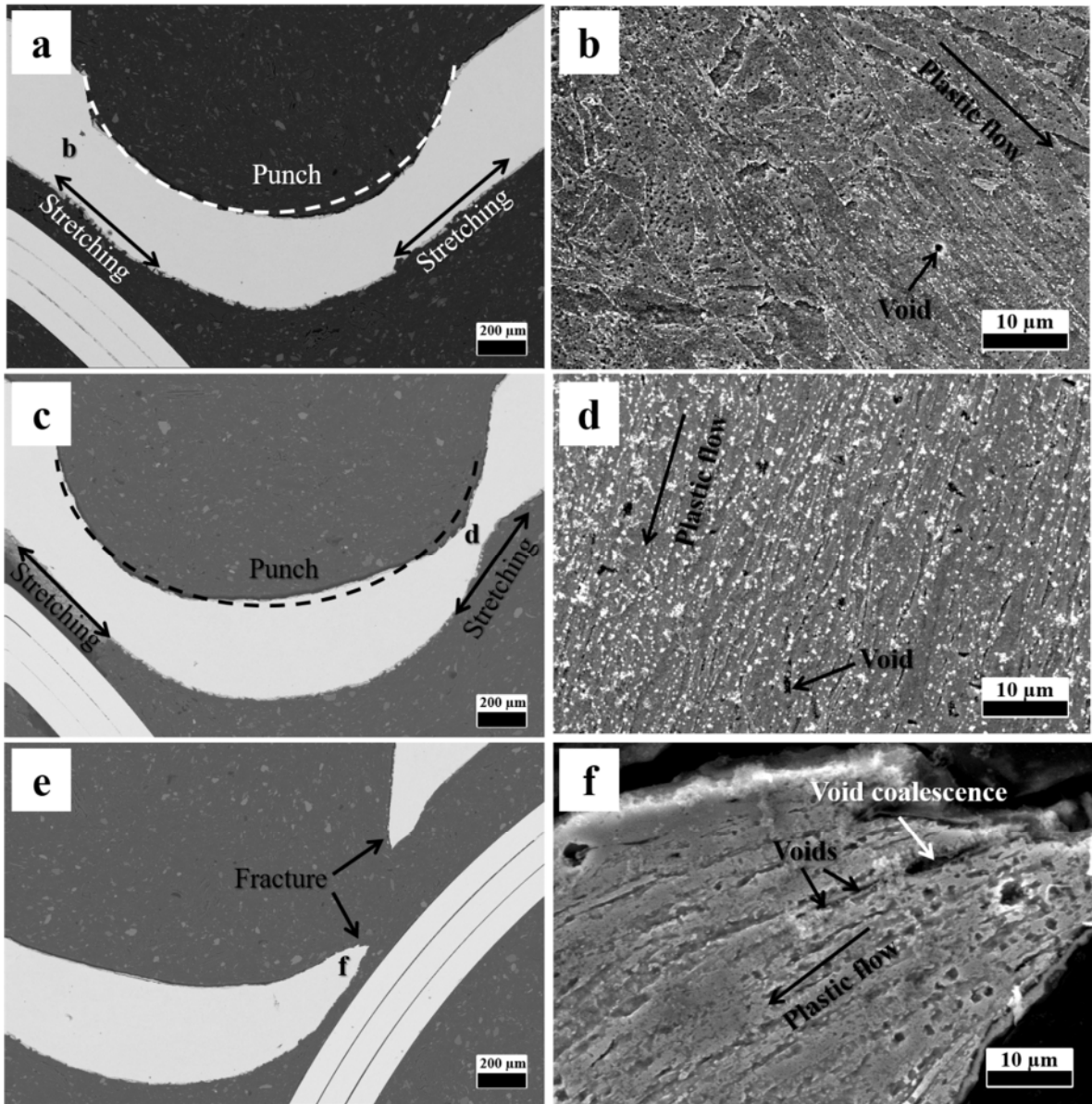
Figure 8. The SEM-SE images showing the cross-sectional microstructure of the deformed specimens at interrupted displacements of 1.5 mm (a and b), 1.65 mm (c and d) and 1.74 mm (e and f).
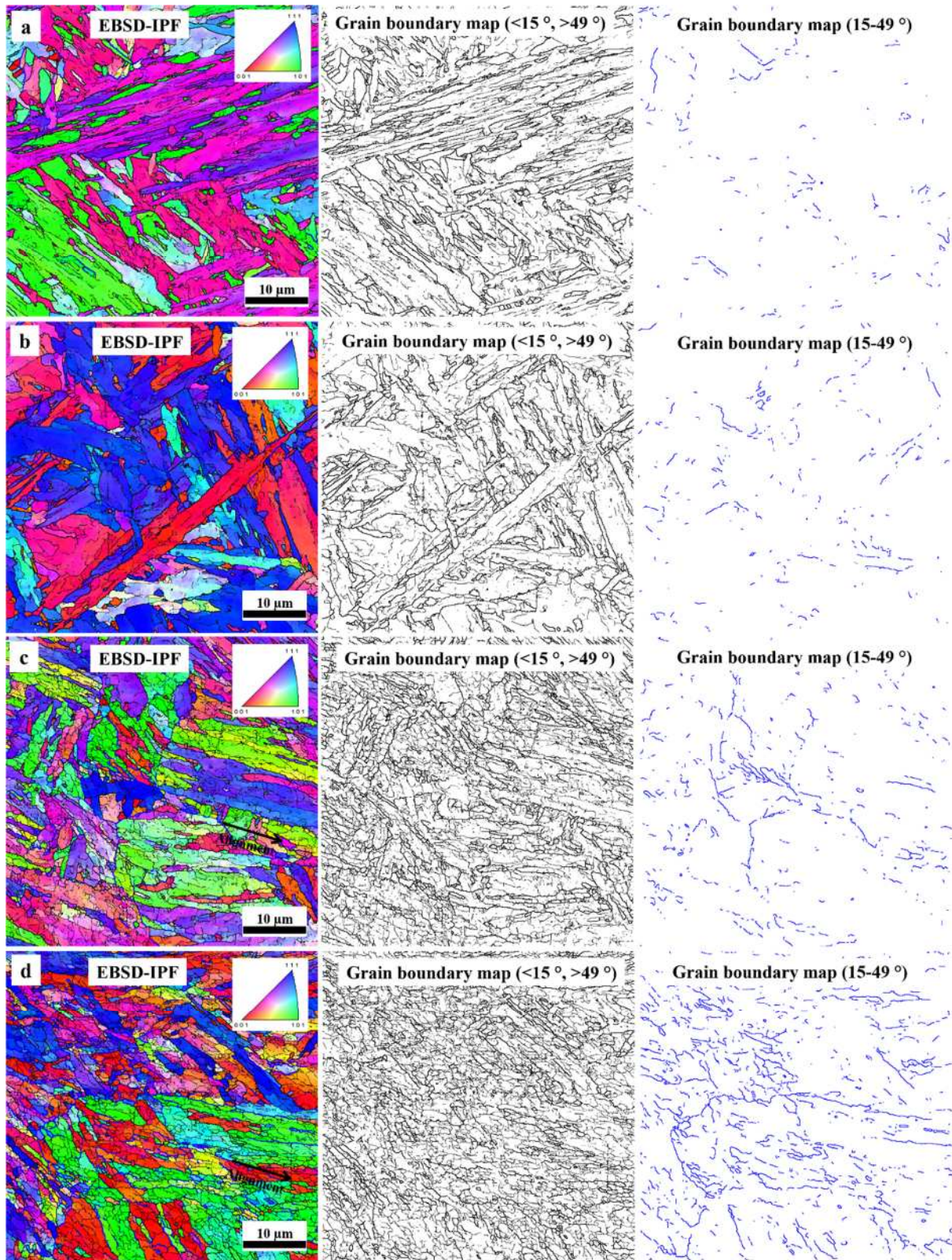
Figure 9. The EBSD Inverse Pole Figure (IPF) maps and the corresponding grain boundary maps at misorientations below 15 °, 15-49 ° and above 49 ° for regions near the edge of contact at displacements of 0.26 mm (a), 0.6 mm (b), 1.0 mm (c) and 1.25 mm (d) respectively. The colours in IPF represent the orientations of grains. The grey lines and black lines in the grain boundary map represent the misorientations <15 ° and >49 ° respectively. The blue lines in the grain boundary map represent the misorientations between 15-49 °.
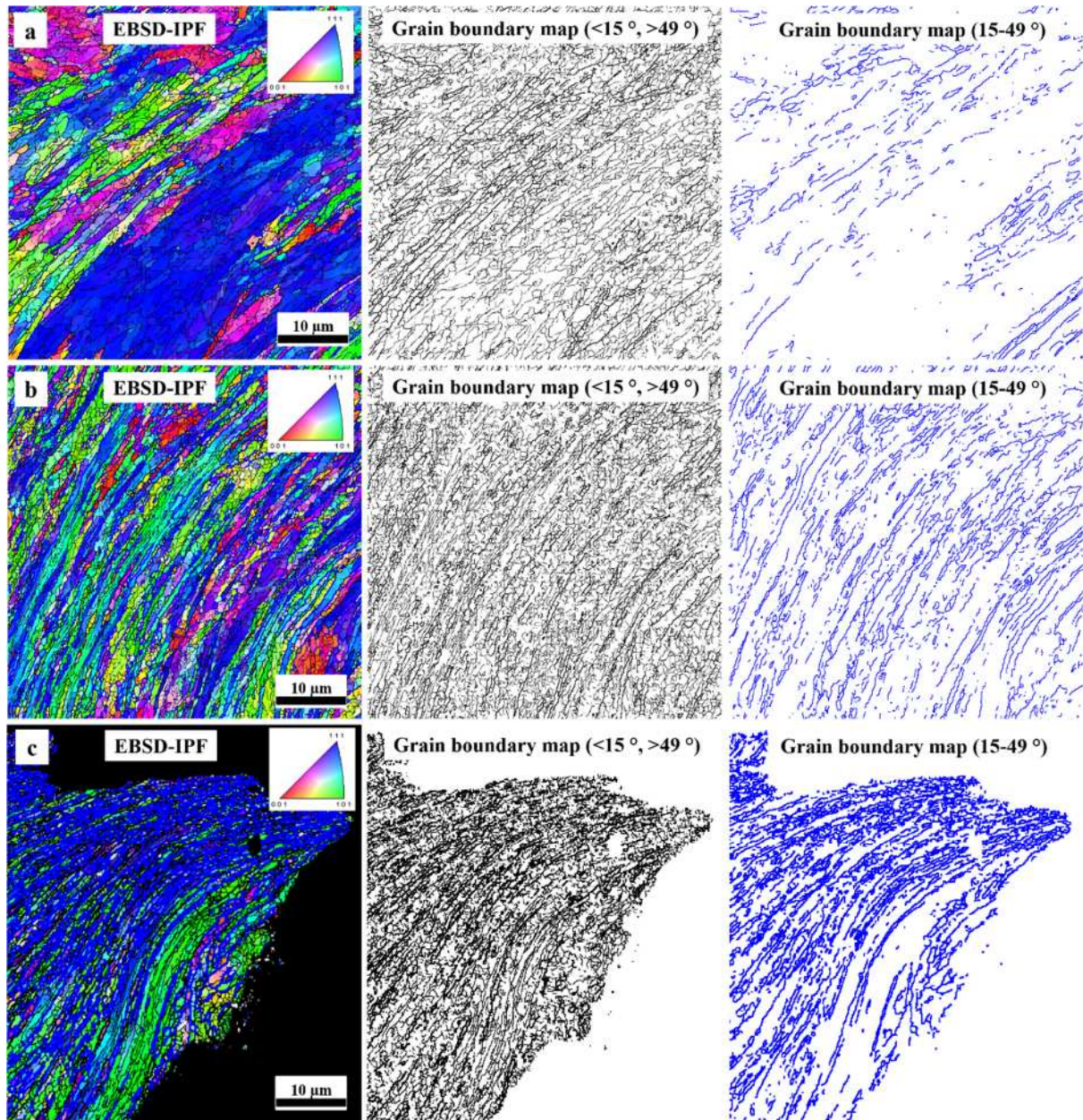
Figure 10. The EBSD Inverse Pole Figure (IPF) maps and the corresponding grain boundary maps at misorientations below 15 °, 15-49 ° and above 49 ° for regions near the edge of contact at SPTT displacements of 1.5 mm (a), 1.65 mm (b) and 1.74 mm (c). The colours in IPF represent the orientations of grains. The grey lines and black lines in the grain boundary map represent the misorientations <15 ° and >49 ° respectively. The blue lines in the grain boundary map represent the misorientations between 15-49 °.
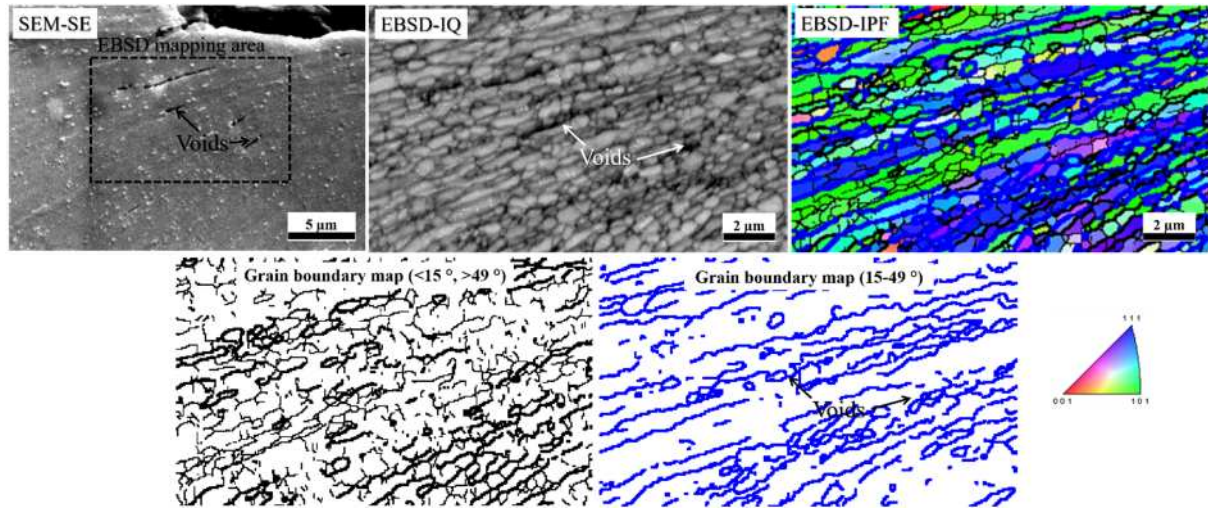
Figure 11. The SEM-SE micrograph of an area close to the fracture tip and the corresponding EBSD Image Quality (IQ) map, Inverse Pole Figure (IPF) map, and the grain boundary maps at misorientations below 15 °, 15-49 ° and above 49 °
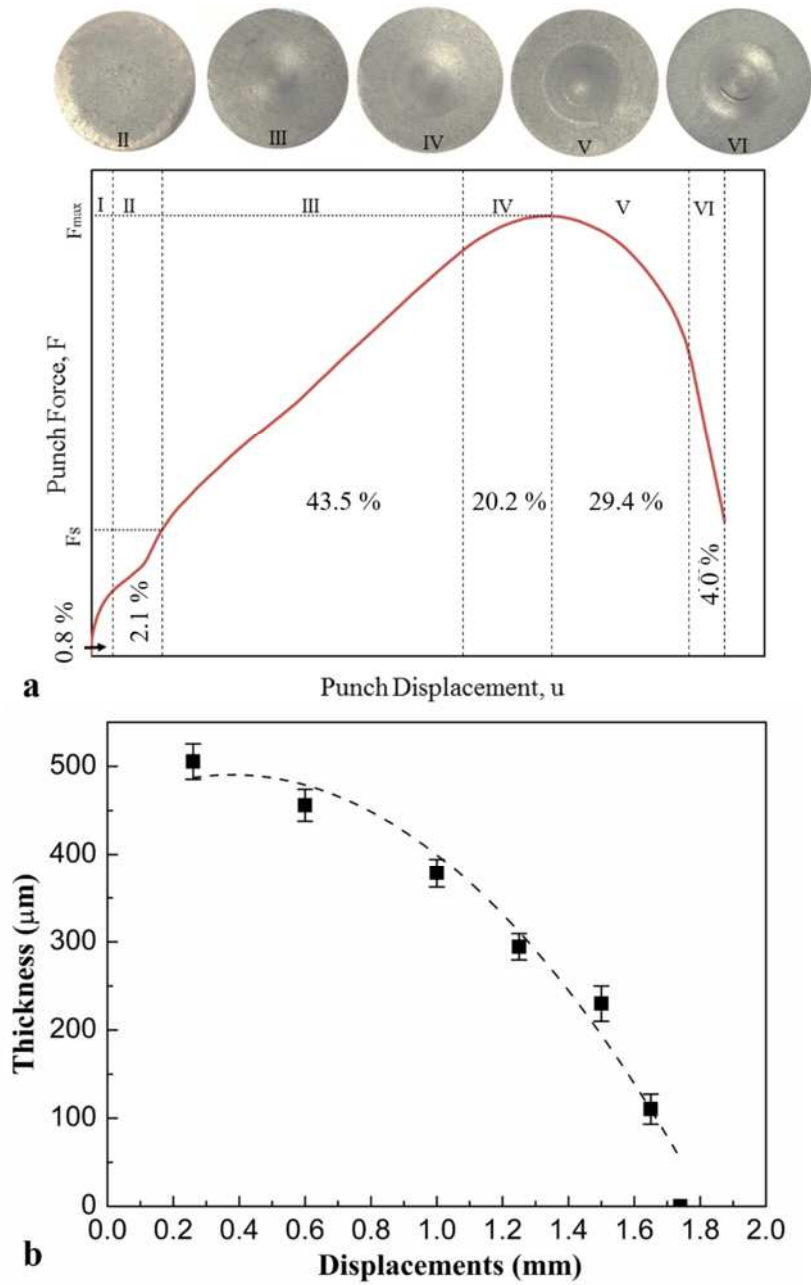
Figure 12. The deformation energy in different stages of the SPTT load-displacement curve for P91 at 600 °C (a) and the evolution of specimen thickness at the edge of contact against displacements (b).
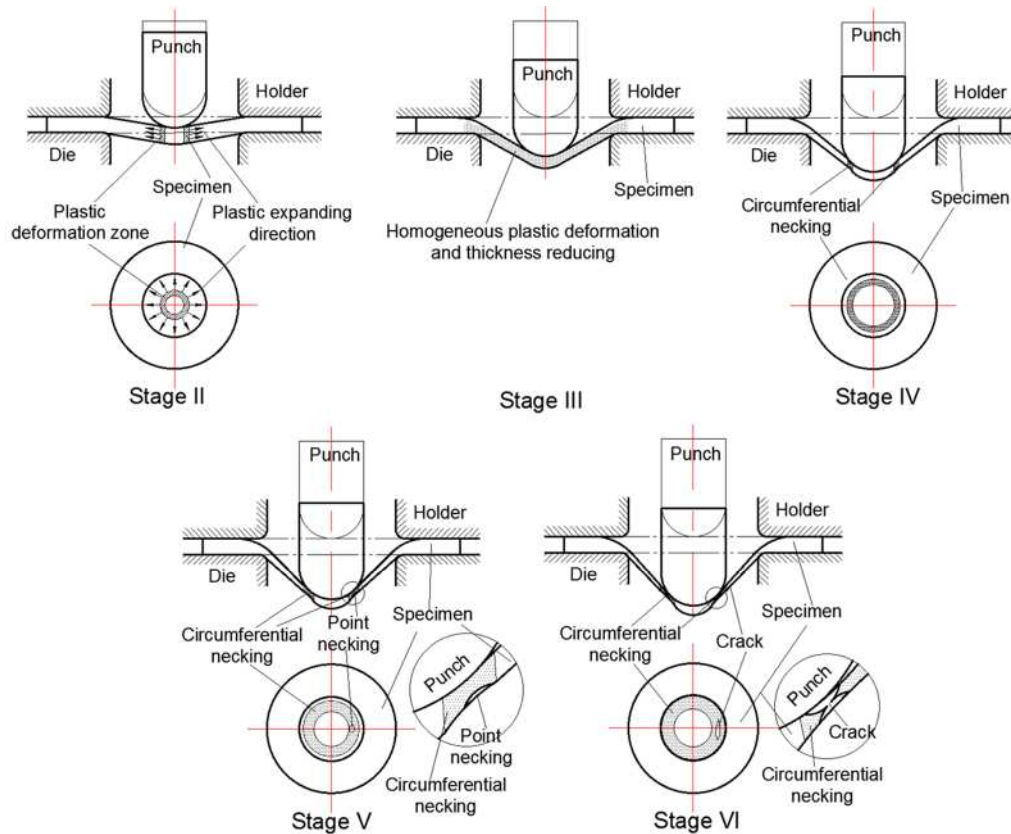
Figure 13. The schematic diagram of deformation mechanism of P91 in SPTT at different stages.
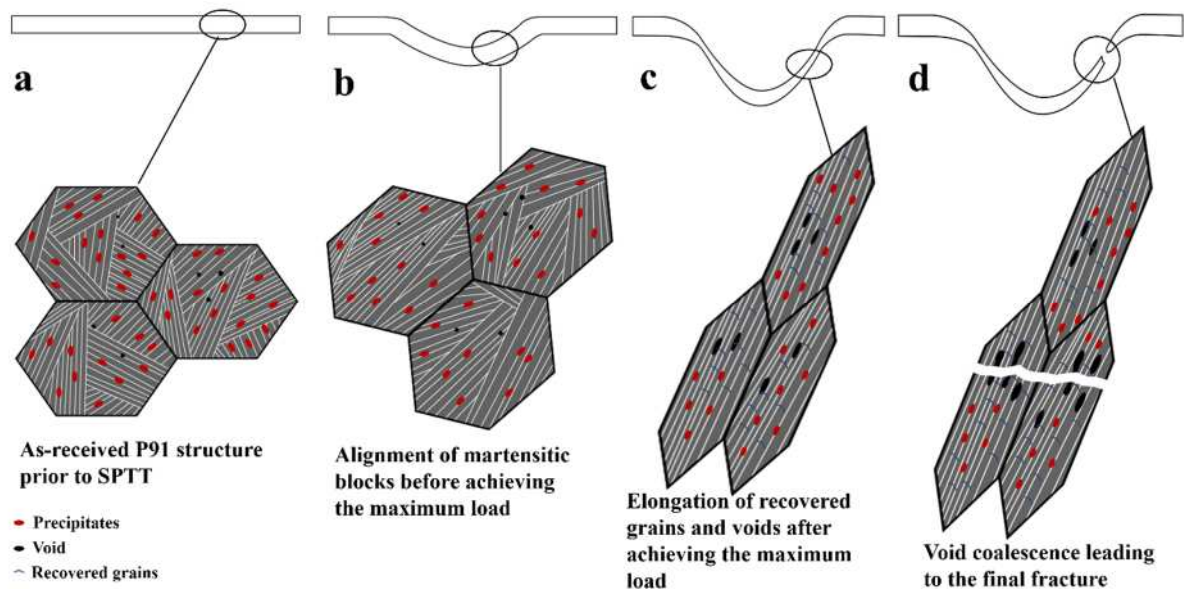
Figure 14. The schematic diagram of microstructure evolution and fracture mechanism of P91 during SPTT. (a) the as-received structure prior to SPTT, (b) the block alignment, (c) the elongation of recovered grains and voids and (d) the void coalescence that leads to fracture.